Received January 29, 2021, accepted February 20, 2021, date of publication March 2, 2021, date of current version March 12, 2021.
Digital Object Identifier 10.1109/ACCESS.2021.3063655

Geometrical-Empirical Channel Propagation Model for Human Presence at 60 GHz

ANMOL BHARDWAJ[1], DEREK CAUDILL[2], CAMILLO GENTILE[1], (Member, IEEE), JACK CHUANG[1], JELENA SENIC[2], AND DAVID G. MICHELSON[3], (Senior Member, IEEE)
[1]Wireless Networks Division, National Institute of Standards and Technology, Gaithersburg, MD 20899, USA
[2]RF Technology Division, National Institute of Standards and Technology, Boulder, CO 80305, USA
[3]Department of Electrical and Computer Engineering, University of British Columbia, Vancouver, BC V6T 1Z4, Canada
Corresponding author: Camillo Gentile (camillo.gentile@nist.gov)

ABSTRACT Previous efforts to develop simulation and/or measurement-based channel propagation models for the effect of human blockage on millimeter-wave communication systems have yielded important results, but lack either accuracy, generality, or simplicity. To fill that void, in this paper we propose a hybrid geometrical-empirical model for human presence; we refer to it as human presence because reflection from the body before and after blockage occurs in addition to diffraction around the body during blockage (as in previous efforts) is incorporated. Specifically, propagation is modeled as the superposition of the main transmission path and reflected and/or diffracted paths from the body; the geometrical component of the model accounts for the phase of each path while the empirical component accounts for its amplitude. To validate the proposed model and extract its empirical parameters, an exhaustive measurement campaign with 120 blockage scenarios, comprising varying human subjects and transmitter-human-receiver configurations, was conducted; a total of 180,000 channel acquisitions was recorded with our precision, state-of-the-art 60-GHz channel sounder. The overall model is shown to be computationally efficient yet general enough to accurately represent a wide range of scenarios.

INDEX TERMS Reflection, diffraction, mmWave, blockage, shadowing event, Doppler.

I. INTRODUCTION

Exploitation of the millimeter-wave (mmWave) bands is a key part of the 5G strategy to address the exponentially growing demand for radio access with high throughput and capacity. One drawback is that mmWave signals are highly susceptible to blockage by people, building structures, etc. [1]–[3]. When the main transmission path is obstructed, communication will be conducted through secondary paths originating from reflection or scattering by the environment. Considerable work to develop simple but accurate models for the effect of human presence on mmWave propagation has been advanced to date: some work has been purely simulation based; other work has integrated measurements to construct empirical models. The ultimate goal of both activities is to provide network engineers with the tools required to assess the impact of human presence on the performance of mmWave communication systems.

In [4], the authors provide a comprehensive summary of models for human blockage. Simulation-based models are mainly divided into two main categories for portraying the body, as an *absorbing screen* or a *conducting screen*. We first consider the former, in which the human body is modeled as a vertical screen with infinitesimal width. In [5], diffraction from both sides of the screen are treated as knife edges in the double knife-edge diffraction (DKED) model. The complex amplitude of the electric field at the receiver is estimated by integrating over the half-plane above the knife edge. Since the human body acts like an absorber, the diffracted fields are not dependent on the polarization of the incident wave. Similar work was presented in [6], where human blockage is modeled by two vertical strips – each with a third diffraction from the top of the strip – in the multiple knife-edge diffraction model. More complex versions of the latter are reported in [6]–[9], where human torso, shoulders, head, and legs are also captured. Although such models can provide very accurate results, because each diffracted path is described through the Fresnel integrals (Section II), repeated use of these integrals results in a computationally intensive model [10].

In the conducting screen model, the Uniform Theory of Diffraction is used estimate fields diffracted from edges of a vertical screen. Specifically, each edge is treated as a wedge

The associate editor coordinating the review of this manuscript and approving it for publication was Danping He.

and the corresponding diffraction coefficients for these perfectly conducting wedges are derived. Other cases include the representation of human body as a conducting circular/elliptical cylinder, where superposition of diffracted rays around the cylinder is calculated using the Geometrical Theory of Diffraction (GTD). Such blockage models have been well established in the literature [11]–[15]. However, these models are somewhat limited to device-to-device (D2D) scenarios only, where the incident wave is perpendicular to the cylinder. They are extremely computationally extensive for device-to-infrastructure (D2I) cases where transmitter (TX) and receiver (RX) have different heights [16]. The solution involves eigenfunction expansion resulting in numerical integration through the Finite-Difference Time-Domain (FDTD) method [16].

Fidelity of electromagnetic simulation-based models is hinged upon verification through measurement. A number of measurement campaigns and resultant modeling efforts have been conducted both to validate and complement simulation-based studies [13], [14], [17]–[33]: Human blockage measurements at 73 GHz are presented in [18] and measured results are compared against the original DKED model and a revised version that accounts for directional antennas. Along the same lines, in [17] measurements were conducted and fit to a popular model described later.

The models proposed to date cover a wide range of complexity: the simplest have a binary representation for either presence or absence of blockage whereas the most complex account for fading observed in the blockage (*shadow*) region through numerical integration. Although these models are indeed accurate, either their range of applicability is geometrically limited or they are computationally intensive. We believe that a tractable and computationally efficient approach is required.

To that end, in this paper we propose a hybrid geometrical-empirical model that exploits the best qualities of both approaches. The complete model for *human presence* goes farther than previous efforts, incorporating reflection from the body *before and after* human blockage occurs in addition to diffraction around the body during blockage; the characteristic behavior of the former event may be exploited by network engineers as a predictive mechanism for the latter, more severe shadowing event. Precision computation of the channel response necessitates accurate knowledge of the complex amplitude (both phase and amplitude) of the corresponding paths; in our case, the geometric component gives accurate estimation of phase while the empirical component derived from measurements gives accurate estimation of amplitude. The resultant model can be used by raytracing engines [35], [36] to simulate individual blockage events.

In order to validate the proposed model and extract its empirical parameters, we conducted an exhaustive measurement campaign with our state-of-the art channel sounder, reporting outcomes and lessons learned along the way. The four main contributions of this paper are:

1. High-quality channel measurements, both in terms of the precision or our 60-GHz channel sounder – providing phase-synchronized complex amplitude with 6.25° standard deviation in phase noise whereas other references for human presence only measure real amplitude – and in the sheer number of channel acquisitions – a total of 180,000 thanks to the rapid capture speed of the sounder (the other work closest to ours has only 22,500 [18]) – to more accurately characterize fading;
2. A modified version of the DKED model that predicts fading 5-20 dB more accurately than the original model currently used widely, essentially with no increase in complexity since it just introduces a *diffraction correction factor* to scale the fading;
3. Confirmation, through analysis of measured Doppler frequency spectra, of the sufficiency of the two knife edges in the DKED model to well represent the fading observed;
4. To our knowledge, the first model for human presence that extends beyond the shadow region, to characterize fading before and after blockage due to reflection from the body through a two-ray model.

The remainder of this paper is developed as follows: Section II describes our channel sounder and the measurement campaign to collect data to support the three models for human presence presented: The model presented in Section III is what we refer to as the *reference model* since it is the mostly widely recognized in the literature; its purpose is to benchmark our data against data collected by others in the past; the other two models presented in Sections IV and V, rather, are novel geometrical-empirical models we propose to more accurately describe human presence in the pre- and post-shadow regions and in the shadow region, respectively, while preserving generality and simplicity; besides model descriptions, each of the three sections also contains model validation and parameter extraction from the measurements. Lastly, overall conclusions are drawn in Section VI.

II. MEASUREMENTS

Channel measurement data for a bevy of shadowing events was collected with our 60-GHz channel sounder. The intention was to validate the three models described later and extract their empirical parameters. Details of the measurement campaign and of the channel sounder are provided here.

A. MEASUREMENT CAMPAIGN

The measurements were conducted in our laboratory environment, void of any movement besides that of the human subject under investigation. A diagram of the set-up is displayed in Fig. 1(a). The transmitter (TX) and receiver (RX) heights were fixed at 1.6 m, corresponding to the D2D scenario, which is the most severe since the direct path is fully obstructed by the body[1] [37]. Note that the D2D

[1]This is in contrast, for example, to the D2I scenario, in which the access point is often attached to the ceiling, nominally at 2.5 m, so the direct path may go unobstructed.

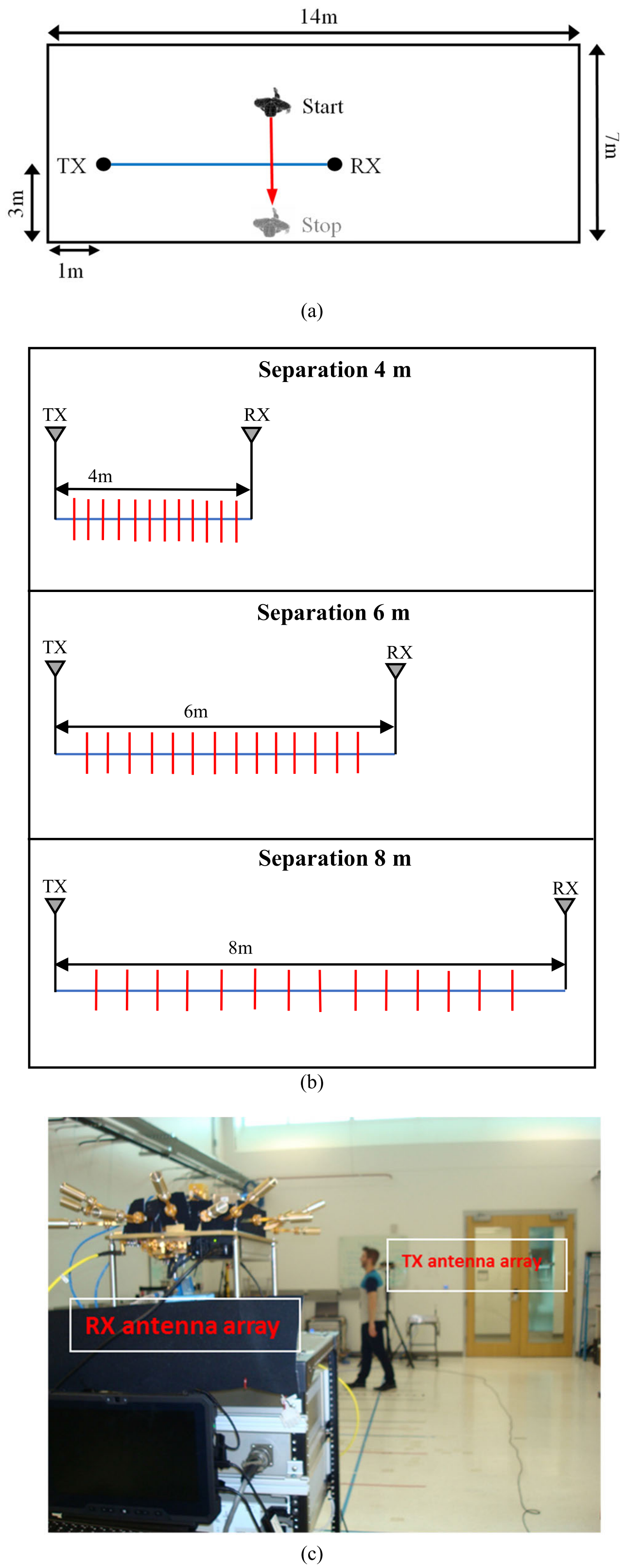

FIGURE 1. **Measurement campaign. (a) Diagram of measurement set-up with human traversing a linear trajectory perpendicular to the direct path between the TX and RX. (b) Assortment of walking trajectories marked with red ticks for each of the three TX-RX separations. (c) Photograph snapped during a measurement with one of the three human subjects.**

scenario is also considered in the other works cited on measurements [13], [14], [17]–[33].

For each measurement scenario, a person traversed a linear trajectory perpendicular to the direct path between the TX and RX. A metronome was employed to facilitate the desired walking speed of 0.3 m/s. Each scenario was identified by three settings:

1. TX-RX separation distance (4m / 6m / 8m);
2. For each separation, a set of displacements of the trajectory along the direct path, illustrated as red ticks in Fig. 1(b); in all, there were 40 displacements across the three separation distances.
3. One of three human subjects with different body structures and heights (1.68 m / 1.72 m / 1.83 m).

In all, there was a total of 120 scenarios. Fig. 1(c) shows a photograph snapped during a measurement with one of the three human subjects. The red tape marks the trajectory displacements along the direct path marked in blue.

B. CHANNEL SOUNDER

NIST's 60-GHz switched array channel sounder [38] is pictured in Fig. 1(c). The TX and RX feature arrays of scalar feed horns, however for this study only one antenna per end was activated. The horns were pointed towards each other along the direct path. The antennas have a Gaussian radiation pattern with 22.5° beamwidth in the azimuth and elevation planes and 18.1-dBi boresight gain. The arbitrary waveform generator at the TX synthesizes a Pseudo Random Bit Sequence (PRBS) of length 2047 and 2 GHz bit rate at baseband, yielding 0.5-ns delay resolution, 33 dB processing gain, and 1023.5-ns delay span. The code is modulated through Binary Phase Shift Keying (BPSK) at an Intermediate Frequency (IF) of 3 GHz. A Local Oscillator (LO) generates the signal at 11.5 GHz frequency. The fifth harmonic of the LO signal was amplified then mixed with the IF signal. The result is an upconverted Radio Frequency (RF) signal at a center frequency of 60.5 GHz that is fed to the TX horn antenna. The TX power was set to 15.7 dBm.

At the RX side, the received signal is downconverted back to 3 GHz IF with the same LO chain: The LO was distributed through a fiber-optic link (gray cable on the floor in Fig. 1(c)) to ensure phase stability. A sample of the phase noise observed across the sweep period is displayed in Fig. 2. The phase noise was quantified to have a standard deviation of 6.25°. The IF signal is directly digitized at 40 GHz and then match filtered to produce the complex channel impulse response (CIR). The noise floor of the receiver is computed as -174 dBm $+ 10\log_{10}(B/Hz) + NF = -76$ dBm, where $B = 2$ GHz and the noise figure (NF) of the low-noise amplifier (LNA) is 5 dB. Combined with the TX power, the antenna gains, and the processing gain of the PRBS signal, the maximum measurable path loss of the system is 148.9 dB for a 12 dB minimum signal-to-noise ratio. A back-to-back calibration was employed to de-embed the RF sections of the TX and RX through pre-distortion filtering.

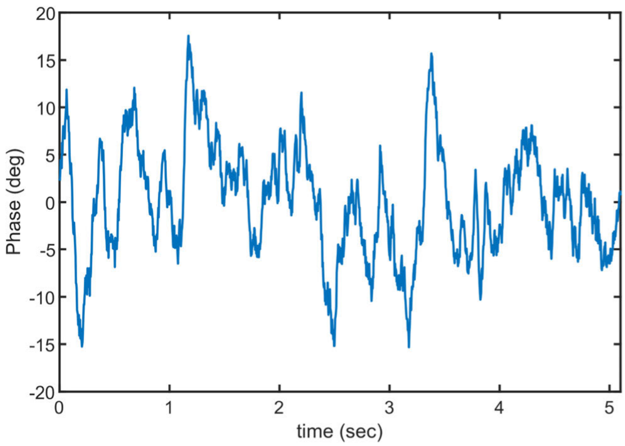

FIGURE 2. Sample of the system phase noise observed over a 5.1s window, equivalent to the channel sweep period.

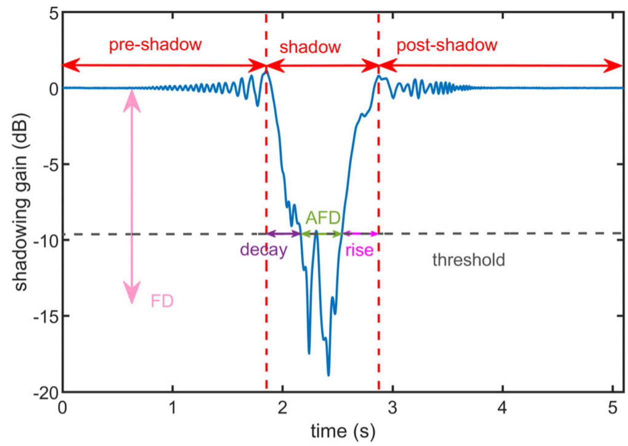

FIGURE 3. Measured signal profile during a shadowing event for an illustrative scenario corresponding to Human C. Also displayed are the parameters of the reference model used to characterize human presence.

Likewise, the angle-of-departure and angle-of-arrival of the direct, reflected, and diffracted paths were estimated from the scenario geometry and pinpointed to the directional patterns of the TX and RX antennas, respectively, to de-embed their gains. What resulted were CIRs that correspond to the ''pristine'' response of the channel alone and not the system. Details of the de-embedment procedures are provided in [38].

A total of 1500 CIRs were captured for each scenario. Thanks to the 0.5-ns delay resolution, individual peaks corresponding to the first path, the ground bounce and reflection from the body when present, and ambient reflections were resolvable in the CIRs. What we refer to as a *channel acquisition* is the complex amplitude of the first path in the CIR; the succession of 1500 acquisitions is what we refer to as the *signal profile* for a measurement scenario. Based on the 0.3 m/s walking speed, the maximum Doppler shift was 120 Hz, yielding the Nyquist sampling duration of 4.2 ms [39]. The actual sampling duration between acquisitions was selected as 3.4 ms and is faster than what was used in similar measurement campaigns [13], [14], [17]–[33]. Such a fast sampling duration enabled precision modeling of fading in the shadow region as well as the damped oscillation in the pre- and post- shadow regions. The sampling duration translated to a total sweep period of 5.1 s over the 1500 acquisitions – long enough to capture the complete shadowing event as the human traversed the trajectory.

III. REFERENCE MODEL FOR THE SHADOW REGION

A. MODEL DESCRIPTION

To our knowledge, all models for human presence to date concentrate solely in the *shadow region*, while the main transmission path is obstructed by the human body. In the reference model [17], the *shadow region* begins with a *decay period*, while the signal gradually loses power as the person approaches, and ends with a *rise period*, while power is restored as the person retreats. The other two parameters of the reference model are *fade depth* (FD) and *average fade duration* (AFD). The parameters are illustrated in Fig. 3 vis-à-vis a signal profile recorded during a shadowing event.

Shadowing gain is defined as the signal power relative to the far end of the profile (normalized to 0 dB) where the profile is completely flat. Fade depth is the maximum attenuation in the profile; the conventional definition is the average value over the center third of the shadow region, but we found this to be somewhat arbitrary since fading is often asymmetric; instead, we reported the average value over the deepest[2] troughs in the profile. The shadow region begins (ends) at highest peak in the profile approaching against (along) the time axis from the trough in the profile. The remaining parameters are based on a pre-defined attenuation threshold: the average fade duration is the period from when the profile first falls below the threshold to when it last rises above it; the decay region is from beginning of the shadow region to when the profile first falls below the threshold; the rise period is from when the profile last falls below the threshold to the end of the shadow region. Values for the parameters reduced from our measurement campaign are presented in IV.A.

B. RESULTS

The empirical parameters of the reference model were extracted from the shadow region of the measured signal profiles. Fig. 4 shows the empirical cumulative distribution function (CDF) for fade depth, which was aggregated from data from all three human subjects and from all trajectories therein (120 shadowing events). The Gaussian, Weibull, and Log-Normal, Gamma, Inverse Gaussian, and Inverse Gamma distribution types were tested against the empirical CDFs to determine which rendered the best fit by way of the Kolmogorov-Smirnov (KS) statistic [40] – a value between 0 and 1 indicating the fit error between two distributions. It was found that the Log-Normal distribution rendered the best fit, as shown in Fig. 4, with the KS statistic reported for each distribution type. Note that the best type passed the null hypothesis at a significance level of 5%, for all model parameters and settings. Table 1 summarizes the model parameters

[2]Based on visual inspection.

TABLE 1. Empirical parameters of the reference model.

	FD (Log-Normal)		AFD (Log-Normal)		Decay (Gamma)	Rise (Log-Normal)
Human A	η = 3.1773, σ = 0.2805	Threshold	2dB	η = -0.3453, σ = 0.1104	a = 5.5229, b = 0.0189	η = -2.4462, σ = 0.3946
			4dB	η = -0.4520, σ = 0.1035	a = 6.3225, b = 0.0195	η = -2.0917, σ = 0.3525
			6dB	η = -0.5563, σ = 0.1100	a = 7.3442, b = 0.0242	η = -1.8793, σ = 0.3166
			8dB	η = -0.6822, σ = 0.1240	a = 7.6221, b = 0.0289	η = -1.6937, σ = 0.3121
Human B	η = 2.8693, σ = 0.3336	Threshold	2dB	η = -0.4490, σ = 0.3035	a = 8.3633, b = 0.0154	η = -2.1037, σ = 0.6335
			4dB	η = -0.6051, σ = 0.2961	a = 8.3816, b = 0.0238	η = -1.8160, σ = 0.5520
			6dB	η = -0.7487, σ = 0.2799	a = 11.2678, b = 0.0202	η = -1.6282, σ = 0.4996
			8dB	η = -0.9220, σ = 0.2617	a = 11.0436, b = 0.0254	η = -1.4704, σ = 0.4744
Human C	η = 2.8942, σ = 0.3405	Threshold	2dB	η = -0.1651, σ = 0.3374	a = 8.2995, b = 0.0148	η = -2.1522, σ = 0.8058
			4dB	η = -0.2814, σ = 0.3313	a = 6.5777, b = 0.0269	η = -1.8191, σ = 0.7235
			6dB	η = -0.3943, σ = 0.3256	a = 8.4308, b = 0.0240	η = -1.5852, σ = 0.6893
			8dB	η = -0.5183, σ = 0.3238	a = 7.9916, b = 0.0300	η = -1.4134, σ = 0.6626
All humans	η = 2.9803, σ = 0.3463	Threshold	2dB	η = -0.2549, σ = 0.2436	a = 6.9512, b = 0.0169	η = -2.2151, σ = 0.5230
			4dB	η = -0.3702, σ = 0.2468	a = 8.0741, b = 0.0198	η = -1.8868, σ = 0.4681
			6dB	η = -0.4891, σ = 0.2454	a = 8.2679, b = 0.0242	η = -1.6681, σ = 0.4504
			8dB	η = -0.6510, σ = 0.3167	a = 8.1379, b = 0.0300	η = -1.4862, σ = 0.4611

derived from all 120 measured shadowing events,[3] displayed per human subject as well as aggregated across all humans.

In the same manner as for fade depth, CDFs for average fade duration, rise period, and decays period were compiled from the data. The optimal CDF distribution types along with their fitted parameters appear in Table 1: the AFD for each case is best described by the Log-Normal distribution while the decay and rise periods are best described by the Gamma and Log-Normal distributions respectively. As expected, the AFD, decay period, and rise period all shorten as the attenuation threshold increases. The results in the table match closely with the work reported by others [6], [17], [18], [14], [21]–[23].

IV. PROPOSED TWO-RAY MODEL FOR THE PRE- AND POST- SHADOW REGIONS

A. MODEL DESCRIPTION

Right before (after) the direct path is obstructed by the human body in the shadow region, the path reflected from the body combines with the direct path in what we refer to as the *pre-shadow* (*post-shadow*) region. The constructive / destructive interference between the two paths is exhibited as damped oscillation; see Fig. 1: As the human approaches, the reflection from the front of the body intensifies, increasing the amplitude of oscillation; vice versa, as the human retreats, the intensity of the reflection from the back of the body diminishes, decreasing the amplitude. Our experiments indicate that the oscillations can be quite strong. Surprisingly, we are aware of no previous efforts to model this behavior. The characteristic behavior of the damped oscillation can act as a precursor to the more intense blockage in the shadow region.

To characterize this behavior, we propose the well-established two-ray ground reflection model [20], substituting the ground bounce for the body reflection. A graphical representation of the proposed two-ray model is shown in Fig. 5, where the human body is represented as a rectangular screen. The associated set of equations follows. The complex amplitude of the direct path is derived from Friis transmission equation[4] as [20]:

$$\alpha_{DIR} = \frac{\lambda}{4\pi d_{DIR}} \cdot e^{\frac{-j2\pi d_{DIR}}{\lambda}}, \tag{1}$$

[3] According to the Central Limit Theorem, a set is statistically sufficient if the number of elements exceeds 30, as it does in our case.

[4] With the transmitter and receiver antenna gains normalized to unity.

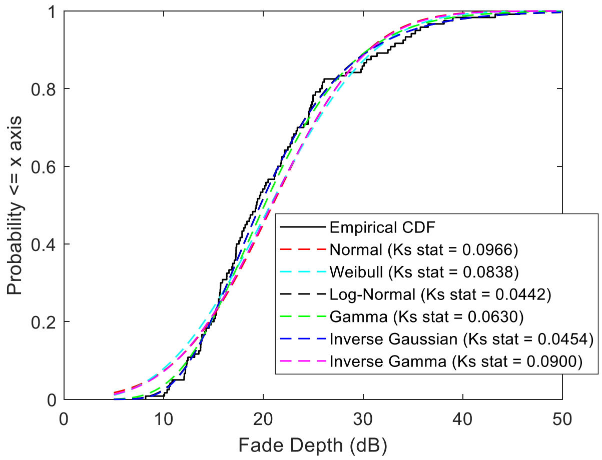

FIGURE 4. Cumulative distribution function (CDF) of fade depth along with three distribution types fit to the empirical CDF.

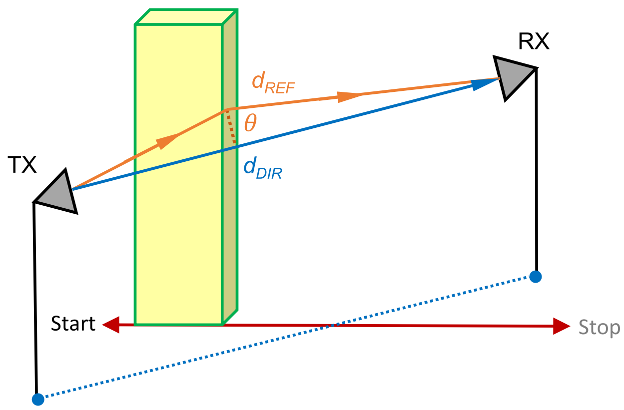

FIGURE 5. Graphical representation of the proposed two-ray model, shown for the pre-shadow region, as the human, portrayed as a rectangular screen, approaches the shadow region. The reflection from the body combines with the direct path.

where λ is the wavelength of the transmitted signal and d_{DIR} is the path length. Similarly, the complex amplitude of the reflected path is [20]:

$$\alpha_{REF} = \frac{\lambda}{4\pi d_{REF}} \cdot \Gamma(\theta) \cdot e^{\frac{-j2\pi d_{REF}}{\lambda}}, \tag{2}$$

where $\Gamma(\theta)$ is the reflection coefficient and d_{REF} is the path length. The reflection coefficient is derived from the Fresnel equations for a flat screen [41],

$$\Gamma(\theta) = \frac{\sin\theta - \sqrt{\epsilon - \cos^2\theta/\epsilon}}{\sin\theta + \sqrt{\epsilon - \cos^2\theta/\epsilon}} + \mathcal{N}(0, \sigma), \tag{3}$$

where θ is incident angle on the screen and ϵ is the complex relative permittivity of the body. A zero-mean Gaussian random variable with standard deviation σ was added to capture irregularities introduced by a non-flat body and swinging limbs. The complex amplitude of the two paths combined is

$$\alpha_{2RAY} = \alpha_{DIR} + \alpha_{REF}. \tag{4}$$

Even though in our measurements the TX and RX were at the same height and the orientation of the human body was perpendicular to the direct path, the two-ray model is nevertheless valid for any antenna heights and body orientation. The path length of the reflection, d_{REF}, just needs to be adjusted to the actual geometry of the scenario and there will also be a non-zero elevation angle in addition to θ. The more general Fresnel equations for (3) can be found in [41].

Whereas all other model parameters are geometrical, the empirical parameters of complex relative permittivity and standard deviation are extracted from the data we collected, as explained in the next section.

TABLE 2. Empirical parameters of the reflection coefficient of the two-ray model.

	$(\epsilon, \sigma\ (dB))$	
	Front	Back
Human A	(0.1 – j2.51, 0.56)	(0.1 – j1.98, 0.39)
Human B	(0.1 – j1.69, 0.44)	(0.1 – j2.10, 0.43)
Human C	(0.1 – j2.91, 0.39)	(0.1 – j3.12, 0.46)
All humans	(0.1 – j2.31, 0.47)	(0.1 – j2.35, 0.43)

B. RESULTS

The two-ray model was fit separately to the pre- and post-shadow regions of the measured signal profiles, per human. First, the reflection coefficient $\Gamma(\theta)$ was estimated from each acquisition α_{2RAY} (see eqs. (1, 2, 4)) in tandem with the reflected path in the pre- and post-shadow regions. Although there was significant overlap between the pulses of the direct and reflected paths, causing the constructive and destructive interference observed, their peaks were distinct, enabling resolution of the paths thanks to the complex-valued profiles. The data was subsequently aggregated over all scenarios per human and over all humans, producing eight rich data sets, displayed as $|\Gamma(\theta)|$ in Fig. 6. Finally, an exhaustive search over ϵ was performed per set to minimize the least-squares fit of eq. (3) to the data, in turn yielding σ. Fig. 6 also displays the fit per set.

Table 2 contains the resultant empirical parameters. The complex relative permittivity between the front and the back of the body were similar, as expected from the symmetrical shadowing events observed. The values between different humans differed more, but nevertheless corresponded well with other works specifically focused on measuring body permittivity [42]. It is interesting to notice in Fig. 6 that at wider incident angles, when the human was farthest from the shadow region, the data in each set tended to branch out – each of the two branches most likely corresponded to a separate swinging arm – giving rise to a larger standard deviation. Though this effect was observed consistently across all eight data sets, it was not modeled explicitly for the sake of simplicity.

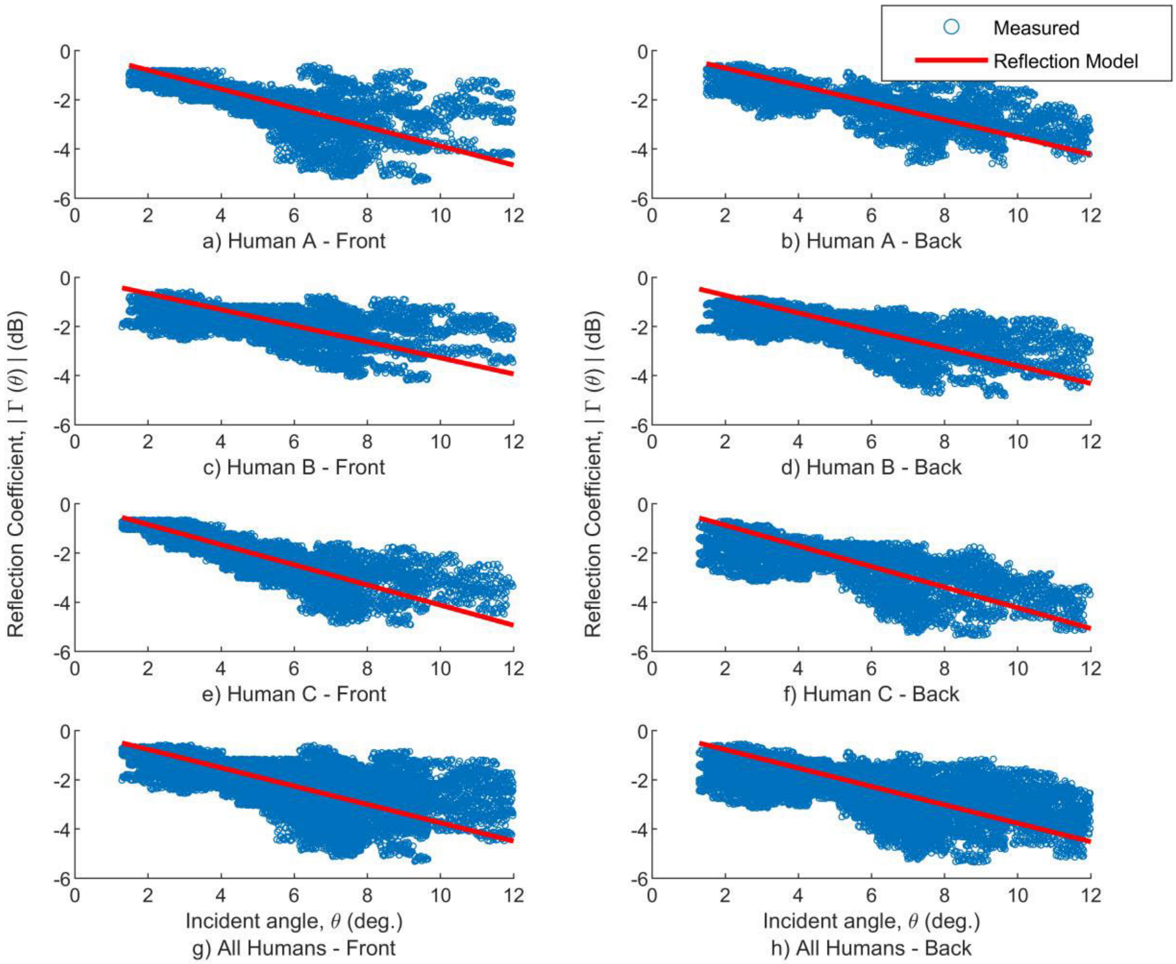

FIGURE 6. Data sets (blue) for the reflection coefficient extracted from the measured signal profiles, aggregated per human and per front or back of the body. The Fresnel model in (3) fit to the data is also shown (red). (a) Human A, front (b) Human A, back (c) Human B, front (d) Human B, back (e) Human C, front (f) Human C, back (g) All humans, front (h) All humans, back.

Fig. 7 shows the illustrative measured profile for Human C from Fig. 3, zoomed in on the pre- and post-shadow regions. In order to substantiate the validity of the two-ray model, also shown is the model realized from equations (1) – (4), with ϵ taken from Table 2 for Human C ($\epsilon = 0.1 - j2.91$ for the pre-shadow region and $\epsilon = 0.1 - j3.12$ for the post-shadow region) and for the nominal case ($\sigma = 0$). As is apparent, the model fits the measurement quite well, and the random deviations are captured in the actual σ values in the table.

V. PROPOSED MODIFIED DKED MODEL (MDKED) FOR THE SHADOW REGION

A. MODEL DESCRIPTION

In this section, we propose a model for fading in the shadow region based on the double knife-edge diffraction (DKED) model for the absorbing screen [5]. As depicted in Fig. 8, the human body is portrayed by an infinitesimally long vertical screen. The direct path is completely absorbed by the body and therefore not accounted for; instead, fading arises from two diffracted paths – one from the front of the body ($n = 1$) and one from the back ($n = 2$) – expressed through the set of equations in the sequel.

The path coefficients for the two non-obstructed half planes are calculated through the Fresnel-Huygens principle according to the geometry in Fig. 8:

$$k_n = \frac{1+j}{2}\left\{\left(\frac{1}{2} - C\left(v_n\right)\right) - j\left(\frac{1}{2} - S\left(v_n\right)\right)\right\},$$
$$v_n = -h_n\sqrt{\frac{2}{\lambda}\left(\left(\frac{1}{d_A}\right) + \left(\frac{1}{d_B}\right)\right)} \tag{5}$$

where $C\left(v_n\right)$ and $S\left(v_n\right)$ are the cosine and sine Fresnel integrals. The superposition of the two paths gives rise to the complex amplitude:

$$\alpha_{DKED} = \frac{\lambda}{4\pi(d_A + d_B)} \cdot \left(k_1 e^{\frac{-j2\pi \Delta d_1}{\lambda}} + k_2 e^{\frac{-j2\pi \Delta d_2}{\lambda}}\right).$$
$$\Delta d_n = \sqrt{h_n^2 + d_A^2} + \sqrt{h_n^2 + d_B^2} \tag{6}$$

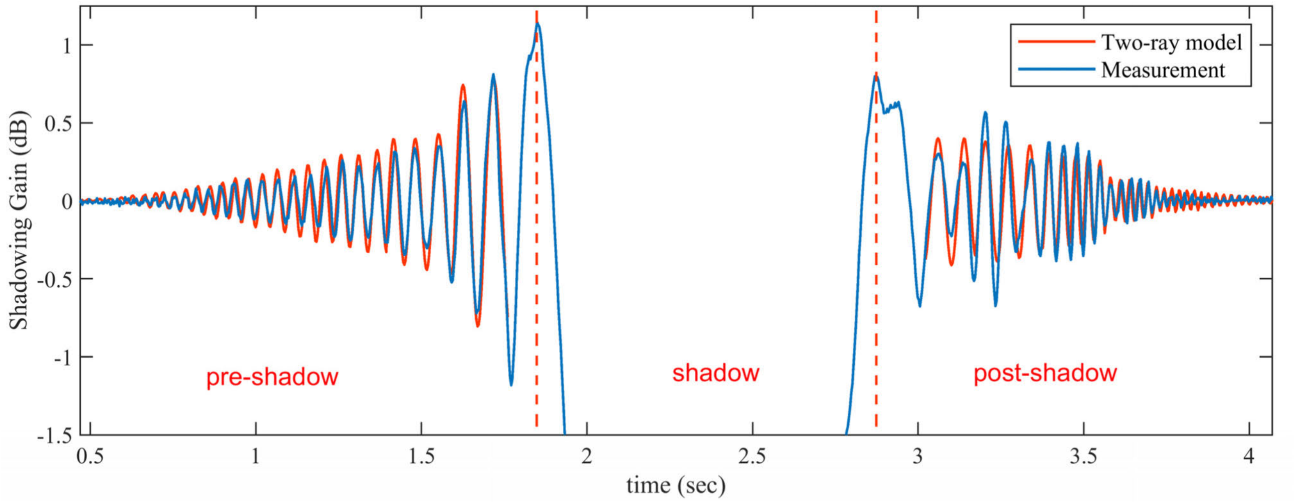

FIGURE 7. Measured signal profile corresponding to the illustrative scenario for Human C from Fig. 3 (blue), zoomed in on the pre- and post-shadow regions. Also shown is a realization of two-ray model (red), substantiating good agreement with the measurement.

As we shall see later, the limitation with the DKED model as presented is that it can severely overshoot the actual fading observed. In order to reconcile any mismatch without increasing the complexity of the model, we introduce a *diffraction correction factor,* γ. The correction factor is applied to (6) as follows:

$$\alpha_{MDKED} = \alpha_{DKED}^{\gamma}. \tag{7}$$

The modified DKED (MDKED) model admits just a fraction of the half-plane power estimated by the original model. The correction factor is estimated empirically through measurement and its range of values is presented in Section V.C.

As the geometry of the two-ray model is valid for any antenna heights and body orientation, so is the KED model, however the equations are slightly more complex than in (5) and (6). The more general equations can be found in [8].

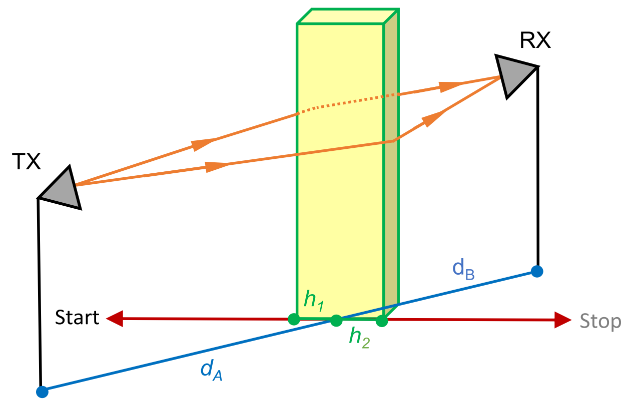

FIGURE 8. Double-edge knife diffraction (DKED) model geometry. The human, portrayed as a rectangular screen, walks along a linear trajectory (red) perpendicular to the direct path (blue). Diffraction around the body (orange) gives rise to the fading observed in the shadow region.

B. MODEL VALIDATION

The purpose of this subsection is to validate the proposed MDKED model. This was accomplished by analyzing the Doppler shift (defined as the rate of phase rotation due to changing path lengths) imparted by the human body. In order to assess the Doppler shift, the short-term Fourier transform of the signal profile using a 100-point window was obtained, equivalent to the window's Doppler frequency spectrum. The window was slid across the time axis one acquisition at a time, resulting in 1401 unique spectra.

The spectra for a select two of the windows within the shadow region are displayed in Fig. 9(a) for the illustrative scenario. The figure clearly demonstrates the existence of two distinct peaks: In the earlier window (acquisition 600-699), the stronger peak is associated with scatter from the front of the body and the weaker peak with scatter from the back; conversely, in the later window (acquisition 640-739) the scatter from the back is stronger than from the front. The crossover in the two peaks therefore occurred between the two windows, precisely at the trough in the signal profile. The Doppler shift of the peaks observed is consistent with the model geometry.

To further validate the model, the Doppler shift of the dominant peak in the spectrum was tracked across the 1401 windows in Fig. 9(b). The quantized values stem from the finite resolution (2.97 Hz) of the discrete Fourier transform. The zero Doppler at the beginning of the profile indicates the static length of the direct path, the only path detected at that time. The subsequent change in Doppler due to front and back scatter is apparent: the person enters the shadow region around acquisition 500, causing the Doppler to drop; in the midst of the shadow region, the Doppler switches sign due to crossover from front to back scatter; thereafter, the Doppler returns to zero as the person retreats. Note that body reflection can also be observed – through the transient magnitude of the dominant peak on the edges of the shadow region – but the Doppler is so miniscule that it is quantized to zero. The double-edge behavior exhibited in Fig. 9(b) was witnessed across all scenarios, supporting the adequacy of the MDKED model – in contrast to more complex models [6], [8], [9] – for

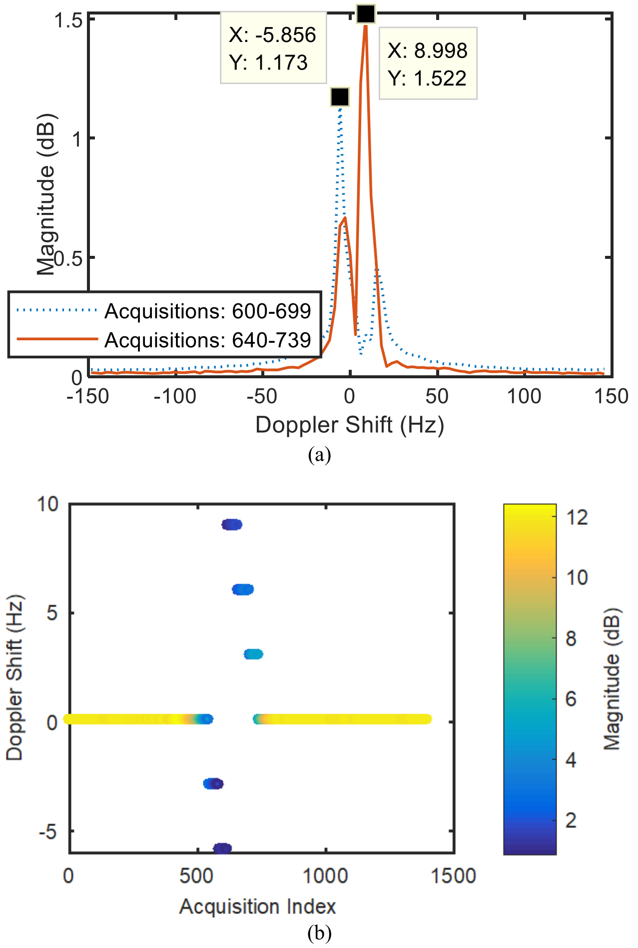

FIGURE 9. **(a) Doppler frequency spectrum for two acquisition windows, showing the crossover from front scatter from the human body (dominant peak in earlier window) to back scatter (dominant peak in later window). (b) The crossover is also apparent when tracking the dominant path across all acquisition windows.**

accurate representation. To our knowledge, no experiments with this level of precision to demonstrate this behavior have been previously reported in the literature.

The adequacy of the MDKED model stems from the 2 GHz bandwidth of the system – the bandwidth expected for 60 GHz systems [43] – corresponding to 0.5 ns delay resolution, or 15 cm path length resolution (given the speed of light). Although in the MDKED model each side of the screen representing the body is treated as a single knife edge, in reality there may be multiple knife edges per side – head, chest, shoulder, arm, etc. – but given their vicinity, the difference in their path lengths is beyond the resolution of the system. Moreover, all knife edges from the same side will have comparable length and since they correspond to the same side will either be increasing or decreasing in unison, so their Doppler shifts will have the same sign and will combine constructively.

C. RESULTS

The empirical parameter of the MDKED model, namely the diffraction correction factor in (7), is extracted in this

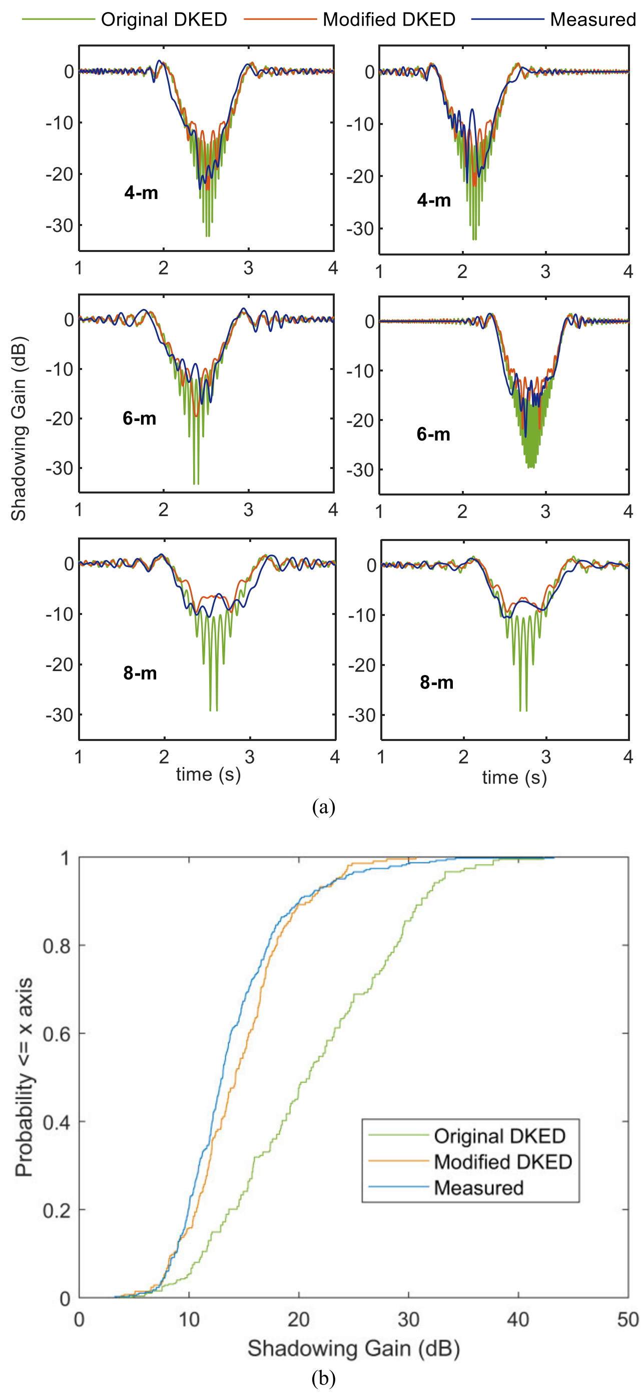

FIGURE 10. **(a) Comparison of the original DKED model to the proposed modified DKED model against signal profiles measured for six illustrative scenarios, two scenarios for each of the three separation distances. (b) CDF of shadowing gain of individual troughs for the original DKED, modified DKED, and measured responses.**

subsection. The original DKED model predicts fading accurately in the decay and rise periods, but often drastically overshoots in between, as supported by our measurements as well as others' [6]; this may be caused by destructive interference between the knife edges. The revision by MacCartney *et al.* [18] in incorporating the antenna patterns improves the overshoot by 1 dB at most. The modified DKED

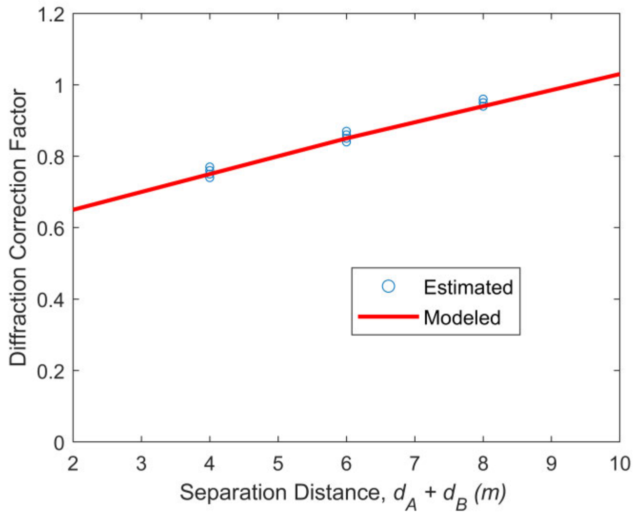

FIGURE 11. Optimal diffraction correction factor corresponding to 4m, 6m, and 8m separation distances (blue) and linear model fit (red).

TABLE 3. Empirical parameters of the diffraction correction factor of the modified DKED model.

	p	q (m^{-1})
Human A	0.560	0.047
Human B	0.540	0.050
Human C	0.540	0.050
All humans	0.560	0.047

model proposed in V.A, rather, achieves much better performance with no detriment to complexity.

The diffraction correction factor of the modified DKED model was estimated per scenario through an exhaustive search to minimize the least-squares fit between (7) and the signal profile in the shadow region. Fig. 10(a) compares the original model (green) with the modified model (red) across six illustrative scenarios, two scenarios for each of the three separation distances; the modified model remarkably decreased overshoot anywhere between 5-20 dB. The overshoot fell mainly at the deep fades within the shadow region. For a comprehensive comparison, the CDFs of the shadowing gain corresponding to individual troughs within the shadow region was computed for the original model, the modified model, and the measured responses across all 120 scenarios; the CDFs are presented in Fig. 10(b). The KS statistic is 0.4850 (large) for the original model with respect to the measured response, yet only 0.1366 (small) for the modified model.

The estimated diffraction correction factor was found to vary negligibly between human subjects – despite the different heights, body shape, skin type, and clothing of each – and between displacements. It was, however, found to vary linearly with separation distance, $d_A + d_B$. In fact, the estimated correction factor for all shadowing events are plotted versus separation distance in Fig. 11. Notice that the data points per separation distance vary little, yet vary significantly across separation distance. The linear model fit to the data points is expressed as:

$$\gamma\,(d_A + d_B) = p + q \cdot (d_A + d_B), \tag{8}$$

with coefficients p and q. The coefficients are provided in Table 3 per human and over all humans, with little variation between the four cases, as suggested earlier.

The model can be used by network engineers to obtain the appropriate diffraction correction factor for a given separation distance. Although we can only vouch for the separation distances measured (4 – 8 m), we expect the model to be valid for at least 2 – 10 m given the clearly linear behavior.

VI. CONCLUSION AND FUTURE WORK

We have proposed a novel geometrical-empirical channel propagation model for human presence, extending previous models for blockage from the body alone to incorporate reflection from the body as well, capturing the complete shadowing event. The model combines the well-established two-ray model for reflection with a modified version of the double knife-edge diffraction model for blockage. The geometrical component of the model enables generalization to a wide range of deployment scenarios while the empirical component ensures fidelity to measurement. An extensive measurement campaign comprising a total of 180,000 channel acquisitions with our state-of-the-art 60-GHz channel sounder was conducted. The purpose was both to validate the proposed model and to extract its empirical parameters.

The two-ray model was demonstrated to fit the data collected over 120 shadowing events very well, and that oscillations in shadowing gain generated by body reflection can be as high as 4 dB, and so cannot be neglected as in the past. Furthermore, analysis for measured Doppler frequency spectra confirmed the sufficiency of two knife edges to well represent the observed diffraction, in contrast to higher-order edges or complex models based on the Geometrical Theory of Diffraction. Finally, the modified version of the diffraction model was shown to fit the data 5-20 dB better than the original version and than a later version that accounts for antenna radiation patterns, essentially with no increase in complexity.

The final product is a computationally efficient model that can accurately represent a wide range of deployment scenarios. For this reason, we believe it will be a valuable tool for those engaged in the design and simulation of mmWave radio-access networks. Notwithstanding, future work can be envisioned to further enhance the generality of the model. For example, measurement campaigns for human presence may be conducted at multiple frequencies and for different polarizations. Lastly, expanding the database to human subjects with more diversity will foster more comprehensive models.

APPENDIX

Equations and parameter definitions corresponding to the distributions used in Table 1 are provided in this section.

A. LOG-NORMAL DISTRIBUTION

The CDF function for a Log-Normal distribution is expressed as [44]:

$$F(x|\mu,\sigma) = \frac{1}{x\sigma\sqrt{2\pi}} \exp\left\{\frac{-(\log x-\mu)^2}{2\sigma^2}\right\}, \quad \text{for } x > 0. \tag{9}$$

Log-normal distribution parameters μ and σ represent that mean and standard deviation of logarithmic values, respectively. They can be derived from the mean m and variance v as:

$$\mu = \log_{10}\left(\frac{m^2}{\sqrt{v+m^2}}\right) \tag{10}$$

$$\sigma = \sqrt{\log_{10}\left(\frac{v}{m^2}+1\right)} \tag{11}$$

B. GAMMA DISTRIBUTION

The CDF function for a Gamma distribution is expressed as [44]:

$$F(x|a,b) = \frac{1}{b^a\Gamma(a)}\int_0^x t^{a-1}e^{-\frac{t}{b}}dt \tag{12}$$

$\Gamma(a)$ is the Gamma function. Gamma distribution parameters a and b represent that shape and scale, respectively.

ACKNOWLEDGMENT

Publication of the United States government, not subject to copyright in the U.S.

REFERENCES

[1] Y. Niu, Y. Li, D. Jin, L. Su, and A. V. Vasilakos, "A survey of millimeter wave communications (mm wave) for 5G: Opportunities and challenges," *Wireless Netw.*, vol. 21, no. 8, pp. 2657–2676, Nov. 2015.

[2] J. Kibilda, A. B. MacKenzie, M. J. Abdel-Rahman, S. K. Yoo, L. G. Giordano, S. L. Cotton, N. Marchetti, W. Saad, W. G. Scanlon, A. Garcia-Rodriguez, D. Lopez-Perez, H. Claussen, and L. A. DaSilva, "Indoor millimeter-wave systems: Design and performance evaluation," *Proc. IEEE*, vol. 108, no. 6, pp. 923–944, Jun. 2020.

[3] L. Zhang, Y. Hua, S. L. Cotton, S. K. Yoo, C. R. C. M. Da Silva, and W. G. Scanlon, "An RSS-based classification of user equipment usage in indoor millimeter wave wireless networks using machine learning," *IEEE Access*, vol. 8, pp. 14928–14943, 2020.

[4] W. Qi, J. Huang, J. Sun, Y. Tan, C.-X. Wang, and X. Ge, "Measurements and modeling of human blockage effects for multiple millimeter wave bands," in *Proc. 13th Int. Wireless Commun. Mobile Comput. Conf. (IWCMC)*, pp. 1604–1609, Jun. 2017.

[5] L. Raschkowski, P. Kyösti, K. Kusume, T. Jämsä, V. Nurmela, and A. Karttunen, "Deliverable D1.4: METIS channel models," METIS, Ericson AB, Stockholm, Sweden, Tech. Rep. ICT-317669-METIS/D1.4, Feb. 2015.

[6] M. Jacob, S. Priebe, A. Maltsev, A. Lomayev, V. Erceg, and T. Kürner, "A ray tracing based stochastic human blockage model for the IEEE 802.11 ad 60 GHz channel model," in *Proc. 5th Eur. Conf. Antennas Propag. (EUCAP)*, pp. 3084–3088, Apr. 2011.

[7] J. Kunisch and J. Pamp, "Ultra-wideband double vertical knife-edge model for obstruction of a ray by a person," in *Proc. IEEE Int. Conf. Ultra-Wideband ICUWB*, vol. 2, Sep. 2008, pp. 17–20.

[8] X. Chen, L. Tien, P. Tang, and J. Zhang, "Modelling of human body shadowing based on 28 GHz indoor measurement results," in *Proc. IEEE 84th Veh. Technol. Conf. (VTC-Fall)*, Sep. 2016, pp. 1–5.

[9] N. Tran, T. Imai, and Y. Okumura, "Study on characteristics of human body shadowing in high frequency bands: Radio wave propagation technology for future radio access and mobile optical networks," in *Proc. IEEE 80th Veh. Technol. Conf. (VTC-Fall)*, Sep. 2014, pp. 1–5.

[10] H. H. Xia and H. L. Bertoni, "Diffraction of cylindrical and plane waves by an array of absorbing half-screens," *IEEE Trans. Antennas Propag.*, vol. 40, no. 2, pp. 170–177, Feb. 1992.

[11] M. Ghaddar, L. Talbi, and T. A. Denidni, "Human body modelling for prediction of effect of people on indoor propagation channel," *Electron. Lett.*, vol. 40, no. 25, pp. 1592–1594, Dec. 2004.

[12] M. Jacob, S. Priebe, T. Kürner, M. Peter, M. Wisotzki, R. Felbecker, and W. Keusgen, "Fundamental analyses of 60 GHz human blockage," in *Proc. 7th Eur. Conf. Antennas Propag. (EuCAP)*, Apr. 2013, pp. 117–121.

[13] M. Ghaddar, L. Talbi, T. A. Denidni, and A. Sebak, "A conducting cylinder for modeling human body presence in indoor propagation channel," *IEEE Trans. Antennas Propag.*, vol. 55, no. 11, pp. 3099–3103, Nov. 2007.

[14] M. Peter, M. Wisotzki, M. Raceala-Motoc, W. Keusgen, R. Felbecker, M. Jacob, S. Priebe, and T. Kürner, "Analyzing human body shadowing at 60 GHz: Systematic wideband MIMO measurements and modeling approaches," in *Proc. 6th Eur. Conf. Antennas Propag. (EUCAP)*, Mar. 2012, pp. 468–472.

[15] C. Gustafson and F. Tufvesson, "Characterization of 60 GHz shadowing by human bodies and simple phantoms," in *Proc. 6th Eur. Conf. Antennas Propag. (EUCAP)*, Mar. 2012, pp. 473–477.

[16] A. G. Aguilar, P. H. Pathak, and M. Sierra-Perez, "A canonical UTD solution for electromagnetic scattering by an electrically large impedance circular cylinder illuminated by an obliquely incident plane wave," *IEEE Trans. Antennas Propag.*, vol. 61, no. 10, pp. 5144–5154, Oct. 2013.

[17] G. R. MacCartney, T. S. Rappaport, and S. Rangan, "Rapid fading due to human blockage in pedestrian crowds at 5G millimeter-wave frequencies," in *Proc. IEEE Global Commun. Conf. (GLOBECOM)*, Dec. 2017, pp. 1–7.

[18] G. R. MacCartney, S. Deng, S. Sun, and T. S. Rappaport, "Millimeter-wave human blockage at 73 GHz with a simple double knife-edge diffraction model and extension for directional antennas," in *Proc. IEEE 84th Veh. Technol. Conf. (VTC-Fall)*, Sep. 2016, pp. 1–6.

[19] S. L. Cotton, "A statistical characterization of shadowed device-to-device communications in an indoor environment," in *Proc. 8th Eur. Conf. Antennas Propag. (EuCAP)*, pp. 3362–3365, Apr. 2014.

[20] T. S. Rappaport, *Wireless Communications: Principles and Practice*, vol. 2. Upper Saddle River, NJ, USA: Prentice-Hall, 1996.

[21] M. Jacob, C. Mbianke, and T. Kürner, "A dynamic 60 GHz radio channel model for system level simulations with MAC protocols for IEEE 802.11 ad," in *Proc. IEEE Int. Symp. Consum. Electron. (ISCE)*, Jun. 2010, pp. 1–5.

[22] X. Zhao, Q. Wang, S. Li, S. Geng, M. Wang, S. Sun, and Z. Wen, "Attenuation by human bodies at 26- and 39.5-GHz millimeter wavebands," *IEEE Antennas Wireless Propag. Lett.*, vol. 16, pp. 1229–1232, 2017.

[23] Q. Wang, X. Zhao, S. Li, M. Wang, S. Sun, and W. Hong, "Attenuation by a human body and trees as well as material penetration loss in 26 and 39 GHz millimeter wave bands," *Int. J. Antennas Propag.*, vol. 2017, Mar. 2017, Art. no. 2961090.

[24] S. Collonge, G. Zaharia, and G. ElZein, "Influence of the human activity on wide-band characteristics of the 60 GHz indoor radio channel," *IEEE Trans. Wireless Commun.*, vol. 3, no. 6, pp. 2396–2406, Nov. 2004.

[25] F. Villanese, N. E. Evans, and W. G. Scanlon, "Pedestrian-induced fading for indoor channels at 2.45, 5.7 and 62 GHz," in *Proc. Veh. Technol. Conf. Fall, IEEE VTS Fall VTC. 52nd Veh. Technol. Conf.*, Boston, MA, USA, Sep. 2000, pp. 43–48.

[26] Y. Huang, A. Charbonneau, L. Talbi, and T. Denidni, "Effect of human body upon line-of-sight indoor radio propagation," in *Proc. Can. Conf. Electr. Comput. Eng.*, Ottawa, ON, Canada, 2006, pp. 1775–1778.

[27] N. Moraitis and P. Constantinou, "Indoor channel measurements and characterization at 60 GHz for wireless local area network applications," *IEEE Trans. Antennas Propag.*, vol. 52, no. 12, pp. 3180–3189, Dec. 2004.

[28] L. Talbi, "Human disturbance of indoor EHF wireless channel," *Electron. Lett.*, vol. 37, no. 22, pp. 1361–1363, Oct. 2001.

[29] P. Marinier, G. Y. Delisle, and C. L. Despins, "Influence of human motion on indoor wireless millimeter-wave channel characteristics," in *Proc. IEEE 47th Veh. Technol. Conf., Technol. Motion*, vol. 2, Phoenix, AZ, USA, May 1997, pp. 979–983.

[30] T. Wu, T. S. Rappaport, and C. M. Collins, "The human body and millimeter-wave wireless communication systems: Interactions and implications," in *Proc. IEEE Int. Conf. Commun. (ICC)*, London, U.K.: Jun. 2015, pp. 2423–2429.

[31] R. J. Weiler, M. Peter, W. Keusgen, and M. Wisotzki, ''Measuring the busy urban 60 GHz outdoor access radio channel,'' in *Proc. IEEE Int. Conf. Ultra-WideBand (ICUWB)*, Paris, France, Sep. 2014, pp. 166–170.
[32] K. Kitao, N. Tran, T. Imai, and Y. Okumura, ''Frequency characteristics of changes in received levels by human body blockage in indoor environment,'' in *Proc. Asia–Pacific Radio Sci. Conf. (URSI AP-RASC)*, Seoul South Korea, Aug. 2016, pp. 373–376.
[33] M. Nakamura, M. Sasaki, M. Inomata, and T. Onizawa, ''The effect of human body blockage to path loss characteristics in crowded areas,'' in *Proc. Int. Symp. Antennas Propag. (ISAP)*, Okinawa, Japan, Oct. 2016, pp. 218–219.
[34] *Study on Channel Model for Frequencies From 0.5 to 100 GHz (Release 14)*, document V. 14.3.0, 3GPP, Jan. 2018. Accessed: Aug. 24, 2018. [Online]. Available: https://portal.3gpp.org/desktopmodules/Specifications/Specification-Details.aspx?specificationId=3173
[35] Y. Corre, Y. Lostanlen, and Y. L. Helloco, ''A new approach for radio propagation modeling in urban environment: Knife-edge diffraction combined with 2D ray-tracing,'' in *Proc. Veh. Technol. Conf., IEEE 55th Veh. Technol. Conf. (VTC Spring)*, vol. 1, Birmingham, AL, USA, May 2002, pp. 507–511.
[36] T. V. Nguyen, E. Masry, and L. B. Milstein, ''Channel model and performance analysis of QAM multiple antenna systems at 60-GHz in the presence of human activity,'' in *Proc. IEEE Global Telecommun. Conf. (GLOBECOM)*, Kathmandu, Nepal, Dec. 2011, pp. 1–6.
[37] D. Singh, A. Chattopadhyay, and S. C. Ghosh, ''Distributed relay selection in presence of dynamic obstacles in millimeter wave D2D communication,'' in *Proc. IEEE Int. Conf. Commun. (ICC)*, Dublin, Ireland, Jun. 2020, pp. 1–6.
[38] R. Sun, P. B. Papazian, J. Senic, Y. Lo, J.-K. Choi, K. A. Remley, and C. Gentile, ''Design and calibration of a double-directional 60 GHz channel sounder for multipath component tracking,'' in *Proc. 11th Eur. Conf. Antennas Propag. (EuCAP)*, Mar. 2017, pp. 3336–3340.
[39] A. F. Molisch, *Wireless Communications*, vol. 34. Hoboken, NJ, USA: Wiley, 2012.
[40] N. Smirnov, ''Table for estimating the goodness of fit of empirical distributions,'' *Ann. Math. Statist.*, vol. 19, no. 2, pp. 279–281, Jun. 1948.
[41] C. Gentile, F. Valoit, and N. Moayeri, ''A raytracing model for wireless propagation in tunnels with varying cross section,'' in *Proc. IEEE Global Commun. Conf. (GLOBECOM)*, Dec. 2012, pp. 5027–5032.
[42] D. K. Ghodgaonkar, O. P. Gandhi, and M. F. Iskander, ''Complex permittivity of human skin in vivo in the frequency band 26.5-60 GHz,'' in *Proc. IEEE Antennas Propag. Soc. Int. Symp.*, Salt Lake City, UT, USA, Jul. 2000, pp. 1100–1103.
[43] *Status of Project IEEE 802.11ay*. Accessed: Jan. 3, 2020. [Online]. Available: https://www.ieee802.org/11/Reports/tgay_update.htm
[44] M. Abramowitz and I. A. Stegun, *Handbook of Mathematical Functions With Formulas, Graphs, and Mathematical Tables*, 9th ed. New York, NY, USA: Dover, 1972.

ANMOL BHARDWAJ received the B.A.Sc. and M.A.Sc. degrees in electrical and computer engineering from the University of British Columbia, Vancouver, BC, Canada. From October 2017 to December 2018, he worked as a Guest Researcher with the Communications Technology Laboratory, National Institute of Standards and Technology. Since November 2019, he has been with the Communications Technology Laboratory, National Institute of Standards and Technology. His research interests include millimeter-wave channel measurements and modeling.

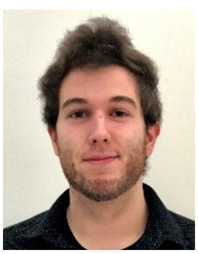

DEREK CAUDILL received the B.S. degree in electrical engineering and the M.S. degree in electrical and computer engineering from the University of Massachusetts Amherst, in 2016 and 2017, respectively. He was a Researcher with the Communications Technology Laboratory, NIST, he supports the data acquisition efforts of mmWave channel model measurements and the systems that such measurements depend on.

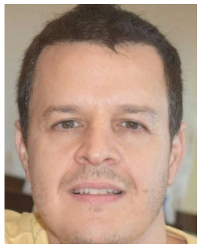

CAMILLO GENTILE (Member, IEEE) received the Ph.D. degree in electrical engineering from Pennsylvania State University, in 2001, with a dissertation on computer vision and artificial intelligence. He joined the National Institute of Standards and Technology, Gaithersburg, MD, USA, in 2001, where he is currently a Project Leader with the Communications Technology Laboratory, Wireless Networks Division. He has authored over 80 peer-reviewed journal and conference papers, a book on geolocation techniques, and a book on millimeter-wave channel modeling. His current interests include channel modeling and physical-layer modeling for 5G communications systems.

JACK CHUANG received the Ph.D. degree from the Communications and Space Sciences Laboratory (CSSL), Pennsylvania State University, in 2008. He was a Graduate Research Assistant with CSSL, Pennsylvania State University. He then worked with BAE Systems in electronic warfare and Cisco Systems in spectrum sharing. He is currently with the Communication Technology Laboratory, NIST, Gaithersburg, MD, USA, developing 5G mmWave channel sounders.

JELENA SENIC received the B.S. and M.S. degrees in electrical engineering from the School of Electrical Engineering, University of Belgrade, Serbia, in 2009 and 2010, respectively. Since January 2015, she has been a Guest Researcher with NIST. Her current research interests include millimeter-wave communications, measurements of signal propagation, and channel modeling for 5G. The team in which she works received the Best Measurement Paper Award at EuCAP 2017.

DAVID G. MICHELSON (Senior Member, IEEE) received the B.Sc., M.Sc., and Ph.D. degrees in electrical engineering from the University of British Columbia (UBC), Vancouver, BC, Canada. From 1996 to 2001, he worked as a member of a joint team from AT&T Wireless Services, Redmond, WA, USA, and AT&T LabsResearch, Red Bank, NJ, USA, where he contributed to the development of propagation and channel models for the next generation and fixed wireless systems. Since 2003, he has been leading the Radio Science Laboratory, Department of Electrical and Computer Engineering, UBC. He worked as a Guest Researcher with the Wireless Network Division, U.S. National Institute of Standards and Technology, in 2018. His research interests include propagation and channel modeling, and wireless communications for connected and automated vehicles, advanced marine systems, and small satellites. He currently serves as a member of the Board of Governors and Chair of the Propagation Committee of the IEEE Vehicular Technology Society. He and a former student received the R.W.P. King Best Paper Award from the IEEE Antennas and Propagation Society, in 2011. He also serves as a Chair of the Canadian National Committee of the International Union of Radio Science, from 2018 to 2021, and the Canadian Representative to URSI Commission F-Wave Propagation and Remote Sensing, from 2015 to 2021.